AFRL-RB-WP-TP-2010-3026

HIGH-FIDELITY SIMULATIONS OF MOVING AND FLEXIBLE AIRFOILS AT LOW REYNOLDS NUMBERS (POSTPRINT)

Miguel R. Visbal, Raymond E. Gordnier, and Marshall C. Galbraith

Computational Aerophysics Branch
Aeronautical Sciences Division

FEBRUARY 2010

STINFO COPY

AIR FORCE RESEARCH LABORATORY
AIR VEHICLES DIRECTORATE
WRIGHT-PATTERSON AIR FORCE BASE, OH 45433-7542
AIR FORCE MATERIEL COMMAND
UNITED STATES AIR FORCE

REPORT DOCUMENTATION PAGE

Form Approved
OMB No. 0704-0188

The public reporting burden for this collection of information is estimated to average 1 hour per response, including the time for reviewing instructions, searching existing data sources, searching existing data sources, gathering and maintaining the data needed, and completing and reviewing the collection of information. Send comments regarding this burden estimate or any other aspect of this collection of information, including suggestions for reducing this burden, to Department of Defense, Washington Headquarters Services, Directorate for Information Operations and Reports (0704-0188), 1215 Jefferson Davis Highway, Suite 1204, Arlington, VA 22202-4302. Respondents should be aware that notwithstanding any other provision of law, no person shall be subject to any penalty for failing to comply with a collection of information if it does not display a currently valid OMB control number. **PLEASE DO NOT RETURN YOUR FORM TO THE ABOVE ADDRESS.**

1. REPORT DATE *(DD-MM-YY)*	2. REPORT TYPE	3. DATES COVERED *(From - To)*
February 2010	Journal Article (Postprint)	01 October 2007 – 31 December 2008

4. TITLE AND SUBTITLE
HIGH-FIDELITY SIMULATIONS OF MOVING AND FLEXIBLE AIRFOILS AT LOW REYNOLDS NUMBERS (POSTRPRINT)

5a. CONTRACT NUMBER
In-house

5b. GRANT NUMBER

5c. PROGRAM ELEMENT NUMBER
61102F

6. AUTHOR(S)
Miguel R. Visbal, Raymond E. Gordnier, and Marshall C. Galbraith

5d. PROJECT NUMBER
2307

5e. TASK NUMBER
N/A

5f. WORK UNIT NUMBER
A04Y0D

7. PERFORMING ORGANIZATION NAME(S) AND ADDRESS(ES)
Computational Aerophysics Branch, Aeronautical Sciences Division
Air Vehicles Directorate
Wright-Patterson Air Force Base, OH 45433-7542
Air Force Materiel Command, United States Air Force

8. PERFORMING ORGANIZATION REPORT NUMBER
AFRL-RB-WP-TP-2010-3026

9. SPONSORING/MONITORING AGENCY NAME(S) AND ADDRESS(ES)
Air Force Research Laboratory
Air Vehicles Directorate
Wright-Patterson Air Force Base, OH 45433-7542
Air Force Materiel Command
United States Air Force

10. SPONSORING/MONITORING AGENCY ACRONYM(S)
AFRL/RBAC

11. SPONSORING/MONITORING AGENCY REPORT NUMBER(S)
AFRL-RB-WP-TP-2010-3026

12. DISTRIBUTION/AVAILABILITY STATEMENT
Approved for public release; distribution unlimited.

13. SUPPLEMENTARY NOTES
PAO Case Number and clearance date: 88ABW-2008-1408, Cleared 7 Jan 2009. This document contains color.

14. ABSTRACT
The present paper highlights results derived from the application of a high-fidelity simulation technique to the analysis of low-Reynolds-number transitional flows over moving and flexible canonical configurations motivated by small natural and man-made flyers. This effort addresses three separate fluid dynamic phenomena relevant to small fliers, including: laminar separation and transition over a stationary airfoil, transition effects on the dynamic stall vortex generated by a plunging airfoil, and the effect of flexibility on the flow structure above a membrane airfoil. The specific cases were also selected to permit comparison with available experimental measurements. First, the process of transition on a stationary SD7003 airfoil section over a range of Reynolds numbers and angles of attack is considered. Prior to stall, the flow exhibits a separated shear layer which rolls up into spanwise vortices. These vortices subsequently undergo spanwise instabilities, and ultimately breakdown into fine-scale turbulent structures as the boundary layer reattaches to the airfoil surface. In a time-averaged sense, the flow displays a closed laminar separation bubble which moves upstream and contracts in size with increasing angle of attack for a fixed Reynolds number. For a fixed angle of attack, as the Reynolds number decreases, the laminar separation bubble grows in vertical extent producing a significant increase in drag. For the lowest Reynolds number considered ($Re_c = 10^4$), transition does not occur over the airfoil at moderate angles of attack prior to stall. Next, the impact of a prescribed high-frequency small-amplitude plunging motion on the transitional flow over the SD7003 airfoil is investigated. The motion-induced high angle of attack results in unsteady separation in the leading edge and in the formation of dynamic-stall-like vortices which convect downstream close to the airfoil. At the lowest value of Reynolds number ($Re_c = 10^4$), transition effects are observed to be minor and the dynamic stall vortex system remains fairly coherent. For $Re_c = 4 \times 10^4$, the dynamic-stall vortex system is laminar at is inception, however shortly afterwards, it experiences an abrupt breakdown associated with the onset of spanwise instability effects. The computed phased-averaged structures for both values of Reynolds number are found to be in good agreement with the experimental data. Finally, the effect of structural compliance on the unsteady flow past a membrane airfoil is investigated. The membrane deformation results in mean camber and large fluctuations which improve aerodynamic performance. Larger values of lift and a delay in stall are achieved relative to a rigid airfoil configuration. For $Re_c = 4.85 \times 10^4$, it is shown that correct prediction of the transitional process is critical to capturing the proper membrane structural response.

15. SUBJECT TERMS

16. SECURITY CLASSIFICATION OF:			17. LIMITATION OF ABSTRACT:	18. NUMBER OF PAGES	19a. NAME OF RESPONSIBLE PERSON (Monitor)
a. REPORT Unclassified	**b. ABSTRACT** Unclassified	**c. THIS PAGE** Unclassified	SAR	22	Miguel R. Visbal **19b. TELEPHONE NUMBER** *(Include Area Code)* N/A

Standard Form 298 (Rev. 8-98)
Prescribed by ANSI Std. Z39-18

RESEARCH ARTICLE

High-fidelity simulations of moving and flexible airfoils at low Reynolds numbers

Miguel R. Visbal · Raymond E. Gordnier ·
Marshall C. Galbraith

Abstract The present paper highlights results derived from the application of a high-fidelity simulation technique to the analysis of low-Reynolds-number transitional flows over moving and flexible canonical configurations motivated by small natural and man-made flyers. This effort addresses three separate fluid dynamic phenomena relevant to small fliers, including: laminar separation and transition over a stationary airfoil, transition effects on the dynamic stall vortex generated by a plunging airfoil, and the effect of flexibility on the flow structure above a membrane airfoil. The specific cases were also selected to permit comparison with available experimental measurements. First, the process of transition on a stationary SD7003 airfoil section over a range of Reynolds numbers and angles of attack is considered. Prior to stall, the flow exhibits a separated shear layer which rolls up into spanwise vortices. These vortices subsequently undergo spanwise instabilities, and ultimately breakdown into fine-scale turbulent structures as the boundary layer reattaches to the airfoil surface. In a time-averaged sense, the flow displays a closed laminar separation bubble which moves upstream and contracts in size with increasing angle of attack for a fixed Reynolds number. For a fixed angle of attack, as the Reynolds number decreases, the laminar separation bubble grows in vertical extent producing a significant increase in drag. For the lowest Reynolds number considered ($Re_c = 10^4$), transition does not occur over the airfoil at moderate angles of attack prior to stall. Next, the impact of a prescribed high-frequency small-amplitude plunging motion on the transitional flow over the SD7003 airfoil is investigated. The motion-induced high angle of attack results in unsteady separation in the leading edge and in the formation of dynamic-stall-like vortices which convect downstream close to the airfoil. At the lowest value of Reynolds number ($Re_c = 10^4$), transition effects are observed to be minor and the dynamic stall vortex system remains fairly coherent. For $Re_c = 4 \times 10^4$, the dynamic-stall vortex system is laminar at is inception, however shortly afterwards, it experiences an abrupt breakdown associated with the onset of spanwise instability effects. The computed phased-averaged structures for both values of Reynolds number are found to be in good agreement with the experimental data. Finally, the effect of structural compliance on the unsteady flow past a membrane airfoil is investigated. The membrane deformation results in mean camber and large fluctuations which improve aerodynamic performance. Larger values of lift and a delay in stall are achieved relative to a rigid airfoil configuration. For $Re_c = 4.85 \times 10^4$, it is shown that correct prediction of the transitional process is critical to capturing the proper membrane structural response.

1 Introduction

Unsteady low-Reynolds-number flows are found in natural flyers, as well as in small unmanned air vehicles and micro air vehicles (or MAV's) due to the relatively small size and low flying speeds involved (Mueller 1985; Shyy 2008; Ellington et al. 1996). Depending upon the specific conditions, these flow fields may be characterized by extensive regions of laminar flow, by the onset of laminar separation bubbles (even at moderate incidence), and by laminar-turbulent transition zones. For the case of flapping wings, as

M. R. Visbal (✉) · R. E. Gordnier · M. C. Galbraith
Computational Sciences Branch, Air Vehicles Directorate,
Air Force Research Laboratory, Wright-Patterson AFB,
OH 45433, USA
e-mail: miguel.visbal@wpafb.af.mil

well as for severe gusts, the highly unsteady forcing induces the formation of dynamic-stall and leading-edge vortices whose evolution and interaction with the aerodynamic surfaces have a significant impact on flight stability and performance. Although much has been studied and learned about these unsteady vortical flow features, challenges still remain in understanding fully their structure, scaling and implications on flight efficiency, in particular over the broad range of parameters encountered.

Vehicle weight considerations in MAV design dictate the use of lightweight and highly flexible or compliant structures. These characteristics create additional complexities due to the rich fluid-structure interactions generated by coupling of aerodynamic, inertial and elastic forces. There is growing recognition that wing deformation may be beneficial to flight performance including stall delay (Smith and Shyy 1995; Shyy and Smith 1997; Song and Breuer 2007; Rojratsirikul et al. 2008; Waszak et al. 2001). However, harnessing these passive effects through aeroelastic tailoring clearly demands further investigation.

From the perspective of analysis and simulation, this non-traditional low-Reynolds-number aerodynamic regime over flexible or flapping surfaces poses a severe challenge due to the following key factors. Difficulties arise due to the presence of highly unsteady flows which defy standard quasi-steady characterization. The flow fields are of a mixed laminar-transitional-turbulent type which high-Reynolds-number analysis tools are not particularly well-suited to handle. Both in nature and in MAV applications, an extensive range of parameters and configurations are encountered. Lastly, there exists a strong coupling of the unsteady aerodynamics and structural response which requires advanced multidisciplinary approaches.

Given the aforementioned difficulties, a heirarchy of increasingly more complex canonical model problems can be considered in order to facilitate progress in the improved understanding and prediction of the multi-disciplinary physics relevant to small flyers. The simplest of these configurations is a maneuvering or flexible airfoil section as a model for flapping flight. In that spirit, the present effort addresses the application of a high-fidelity simulation technique for the analysis of low-Reynolds-number transitional flows over stationary, plunging and flexible airfoils. The methodology, summarized in Sect. 2 and described in more detail elsewhere (Visbal and Rizzetta 2002; Visbal et al. 2003), is based on a 6th-order accurate implicit large-eddy simulation (ILES) procedure incorporating a low-pass spatial numerical filtering technique. The high order algorithm facilitates the proper representation of the transition process whereas the low-pass filter provides regularization in turbulent flow regions in lieu of a standard sub-grid-scale model. This

method is particularly attractive for low-Reynolds-number applications since it permits a seamless treatment of the mixed laminar, transitional and turbulent flow features previously noted.

The first problem considered (Sect. 3) is the detailed structure of the transitional flow over a rigid stationary SD7003 airfoil section. Several experimental and computational studies of this configuration have been performed recently (Ol et al. 2005; Radespiel et al. 2006; Yuan et al. 2005; Lian and Shyy 2006). Although this canonical problem represents perhaps the simple abstraction of low Reynolds number aerodynamics, it exhibits a complex flow physics. Of particular interest here is the process of laminar–turbulent transition over the airfoil associated with the separated shear layer which is present even at modest incidence. In the classical time-averaged representation, this leads to the formation of the so-called laminar separation bubble (LSB) which eventually bursts leading to airfoil stall. The effects of Reynolds number ($10^4 < Re_c = \rho c U_\infty / \mu < 9 \times 10^4$) and angle of attack ($2° < \alpha < 14°$) on the transition process are investigated.

Of more interest to biological and MAV flight, is the aerodynamics of maneuvering airfoils as a tractable model of flapping flight. As a point of departure in this direction, we consider in Sect. 4 the unsteady transitional flow over a plunging SD7003 airfoil. The specific flow and motion parameters correspond to the recent experimental and computational study of McGowan et al. (2008). The airfoil is set at a static angle of attack $\alpha_o = 4°$, and the reduced frequency and plunging amplitude are $k = \pi f c / U_\infty = 3.93$ and $h/c = 0.05$, respectively. These parameters result in a maximum excursion in motion-induced angle of attack of $21.5°$ which promotes through unsteady separation the generation of dynamic-stall-like vortices near the airfoil leading edge. The transitional behavior of these vortices, as they propagate along the airfoil, is investigated for two values of the Reynolds number ($Re_c = 10^4$ and 4×10^4).

Finally, in Sect. 5, we study the impact of structural compliance on the unsteady flow past a stationary flexible airfoil at low Reynolds number. The configuration employed consists of a latex sheet attached to two rigid mounts located at the leading- and trailing-edge of the membrane, and corresponds to the experimental arrangement of Rojratsirikul et al. (2008). The effect of increasing angle of attack on the fluid–structure interaction is examined for a fixed low Reynolds number ($Re_c = 2.5 \times 10^3$). As the membrane deforms due to the aerodynamic load, a cambered geometry is achieved which modifies the stall characteristics of the airfoil. For high incidence, large fluctuations in membrane shape occur which can be viewed as forcing of the separated vortical flow. Limited results on the effect of transition on the flow plast the flexible membrane are also considered for $Re_c = 4.85 \times 10^4$.

2 Methodology

2.1 Governing equations

In the present moving or flexible airfoil simulations, the governing equations are taken to be the full unsteady Navier–Stokes equations cast in strong conservative form and incorporating a general time-dependent curvilinear coordinate transformation $(x, y, z, t) \rightarrow (\xi, \eta, \zeta, \tau)$ (Vinokur 1974; Steger 1978) from physical to computational space. In terms of non-dimensional variables, these equations can be written in vector notation as:

$$\frac{\partial}{\partial \tau}\left(\frac{\vec{U}}{J}\right) + \frac{\partial \hat{F}}{\partial \xi} + \frac{\partial \hat{G}}{\partial \eta} + \frac{\partial \hat{H}}{\partial \zeta} = \frac{1}{Re}\left[\frac{\partial \hat{F}_v}{\partial \xi} + \frac{\partial \hat{G}_v}{\partial \eta} + \frac{\partial \hat{H}_v}{\partial \zeta}\right] \quad (1)$$

where $\vec{U} = \{\rho, \rho u, \rho v, \rho w, \rho E\}$ denotes the solution vector, $J = \partial(\xi, \eta, \zeta, \tau)/\partial(x, y, z, t)$ is the transformation Jacobian, $\hat{F}, \hat{G}$ and $\hat{H}$ are the inviscid fluxes, and $\hat{F}_v, \hat{G}_v$ and $\hat{H}_v$ represent the viscous terms. The full form of these terms can be found, for instance, in Anderson et al. (1984).

It should be noted that the above governing equations correspond to the original *unfiltered* Navier–Stokes equations, and are used without change in laminar, transitional or fully turbulent regions of the flow. Unlike the standard LES approach, no additional sub-grid stress (SGS) and heat flux terms are appended. Instead, a high-order low-pass filter operator (Visbal and Gaitonde 1999; Gaitonde et al. 1999) is applied to the conserved dependent variables during the solution of the standard Navier–Stokes equations. This highly-discriminating filter selectively damps only the evolving poorly resolved high-frequency content of the solution (Visbal and Rizzetta 2002; Visbal et al. 2003). This filtering regularization procedure provides an attractive alternative to the use of standard sub-grid-scale (SGS) models, and has been found to yield suitable results for several turbulent flows on LES level grids. A re-interpretation of this implicit LES (ILES) approach in the context of an approximate deconvolution model (Stolz and Adams 1999) has been provided by Mathew et al. (2003). The ILES approach is very attractive for the present applications involving mixed laminar, transitional and turbulent flow regions.

The structural model for the membrane airfoil is based on the approach of Smith and Shyy (1995) for a two dimensional elastic membrane subjected to a normal force. The governing equation in nondimensional form is

$$\rho_s h \frac{d^2 z}{dt^2} + \rho_s C_d \frac{dz}{dt} - T \frac{d^2 z}{dx^2}\left[1 + \left(\frac{dz}{dx}\right)^2\right]^{-\frac{3}{2}} = \Delta p \quad (2)$$

where

$$T = Eh(\delta_o + \bar{\delta}) \quad (3)$$

$$\bar{\delta} = L - 1 \quad (4)$$

and

$$L = \int_0^1 \sqrt{1 + \left(\frac{dz}{dx}\right)^2}\, dx. \quad (5)$$

In these equations ρ_s, h, C_d, T, E and δ_o are the membrane density, thickness, damping, tension, modulus of elasticity and the length increase of the pretensed membrane, respectively.

2.2 Numerical procedure

All simulations are performed employing the extensively validated high-order Navier–Stokes solver *FDL3DI* (Visbal and Gaitonde 1999; Gaitonde and Visbal 1998). In this code, a finite-difference approach is employed to discretize the governing equations, and all spatial derivatives are obtained using a sixth-order compact-differencing scheme (Lele 1992).

In order to eliminate spurious components, a high-order low-pass spatial filtering technique (Visbal and Gaitonde 1999; Gaitonde et al. 1999) is incorporated. The filter is applied to the conserved variables along each transformed coordinate direction once after each time step or sub-iteration. For transitional and turbulent flows, the previous high-fidelity spatial algorithmic components provide an effective implicit LES approach in lieu of traditional SGS models, as demonstrated in Visbal and Rizzetta (2002) and Visbal et al. (2003).

For the case of a maneuvering airfoil, the grid is moved in a rigid fashion following the prescribed kinematics which provides the position and velocity of the mesh at every instant in time. For the flexible membrane airfoil computations, the aerodynamic mesh is allowed to deform in accordance with the motion of membrane. A simple algebraic method, described in Melville et al. (1997), is used to deform the grid in order to accommodate the instantaneous shape of the membrane. In both situations, great care must be exercised to avoid grid-motion-induced errors. In order to ensure that the geometric conservation law (GCL) is satisfied, the time metric terms are evaluated as described in detail in Visbal and Gaitonde (2002).

The membrane structural equation is solved numerically employing the procedure discussed in Gordnier (2008). Pinned conditions are prescribed at the membrane leading- and trailing-edges. Coupling of the aerodynamics with the membrane response occurs through the imposed pressure force, Δp, in Eq. 2 and by the resulting deflection of the

membrane, which is returned to the aerodynamic grid. A complete synchronization of the aerodynamic and structural systems is achieved through an implicit global subiteration strategy (Gordnier 2008). During each subiteration, the aerodynamic loading in the membrane equations is updated, and the new surface displacements are then provided to the aerodynamic solver. Using this approach, the temporal lag between the aerodynamic and structural solutions, as well as numerical linearization errors may be effectively eliminated.

3 Transitional flow over stationary SD7003 airfoil

In this section, we consider the effect of transition on the flow structure over an airfoil at Reynolds numbers relevant to MAV applications. At low Reynolds numbers ($Re_c = \rho c U_\infty / \mu < 10^5$), the flow may remain laminar over a significant portion of the airfoil, and is unable to sustain even mild adverse pressure gradients. For moderate incidence, separation leads to the formation of a laminar separation bubble (LSB) which breakdowns into turbulence prior to reattachment. The dynamics of this laminar separation bubble, as it moves towards the leading edge with increasing angle of attack and eventually bursts, has a significant impact on airfoil performance.

Results from large-eddy simulations for an SD7003 airfoil are presented. This airfoil geometry was selected since it exhibits a relatively large LSB on the suction side of the airfoil, and since it has been the subject of recent experimental and computational investigations (Shyy 2008; Ol et al. 2005; Radespiel et al. 2006; Yuan et al. 2005; Galbraith and Visbal 2008). Details of the present computations can be found in Galbraith and Visbal (2008) and Galbraith (2009) wherein the effects of grid resolution, Mach number and computational spanwise extent have been explored. Computations were performed for a Reynolds number range $10^4 < Re_c < 9 \times 10^4$, and for angles of attack $2° < \alpha < 14°$.

3.1 Effect of angle of attack

The evolution of the time-averaged flow structure with increasing incidence is examined at a fixed Reynolds number ($Re_c = 6 \times 10^4$). Shown in Fig. 1 are the mean streamline patterns and the Reynolds stress ($u'v'$) contours for several angles of attack. The corresponding mean surface pressure distributions are given in Fig. 2. In addition, Table 1 provides a summary of the locations of laminar separation and turbulent reattachment, as well as the maximum bubble height (defined in terms of the distance from the airfoil surface to the maximum velocity location at the edge of the shear layer). Further information such as

skin-friction coefficient distribution and aerodynamic loads can be found in Galbraith and Visbal (2008).

At $\alpha = 2°$, a long region of laminar separation is observed over the airfoil which closes just upstream of the trailing edge ($x/c = 0.92$). Relatively small values of Reynolds stress magnitude are seen near the reattachment zone. As the angle of attack increases to $\alpha = 4°$, the laminar separation point moves upstream due to the higher adverse pressure gradient it encounters. The reattachment location is also displaced upstream due to the more intense process of transition to turbulence, as reflected in the increased magnitude of Reynolds stress. As a result, the mean separation bubble contracts both in height and in streamwise extent. This overall behavior of the LSB continues as the angle of attack increases up to $\alpha = 11°$. Over this range of incidence, the C_p (Fig. 2) distributions display several well-defined characteristics, including a suction peak, a plateau associated with laminar separation, and a fairly rapid recovery following transition. All of these features are found to become sharper with increasing airfoil incidence. At $\alpha = 14°$, the laminar separation bubble fails to close resulting in so-called bubble bursting. Airfoil stall is evident in the collapse of the suction peak and in an essentially flat pressure distribution over the entire suction surface. A large mean region of recirculation (which extends far away from the airfoil), as well as a reduction in the maximum magnitude of the Reynolds stress are also observed (Fig. 1).

Comparison of the computed time-averaged flow structure with high-resolution experimental measurements is shown in Fig. 3 for $\alpha = 4°$. The measurements denoted as TU-BS correspond to the experiments of Radespiel et al. (2006), whereas the data referred to as HFWT was obtained by Ol et al. (2005). A comparison with experiments in terms of the mean separation bubble characteristics is also provided in Table 2. Good overall agreement is observed between the experimental and computational flow structures. Some discrepancies in specific details exist between the computations and experiment, as well as between the experimental data sets themselves. In particular, the LSB and the region of significant Reynolds stress appear to be larger in the computation relative to experiment. Also, the reported separation locations differ between the two experiments, due in part to the difficulties associated with obtaining the precise separation point from near-wall PIV measurements for a very shallow separation region. It should be noted, that the LSB transition process is expected to be quite sensitive to several factors including freestream turbulence and precise experimental setup (e.g., aspect ratio, interference effects). In the present calculations, no attempt has been made to duplicate any such factors which in general are not well characterized. For instance, no freestream turbulence is imposed on the incoming

Fig. 1 Mean streamline pattern and Reynolds stress as a function of angle of attack for $Re_c = 6 \times 10^4$
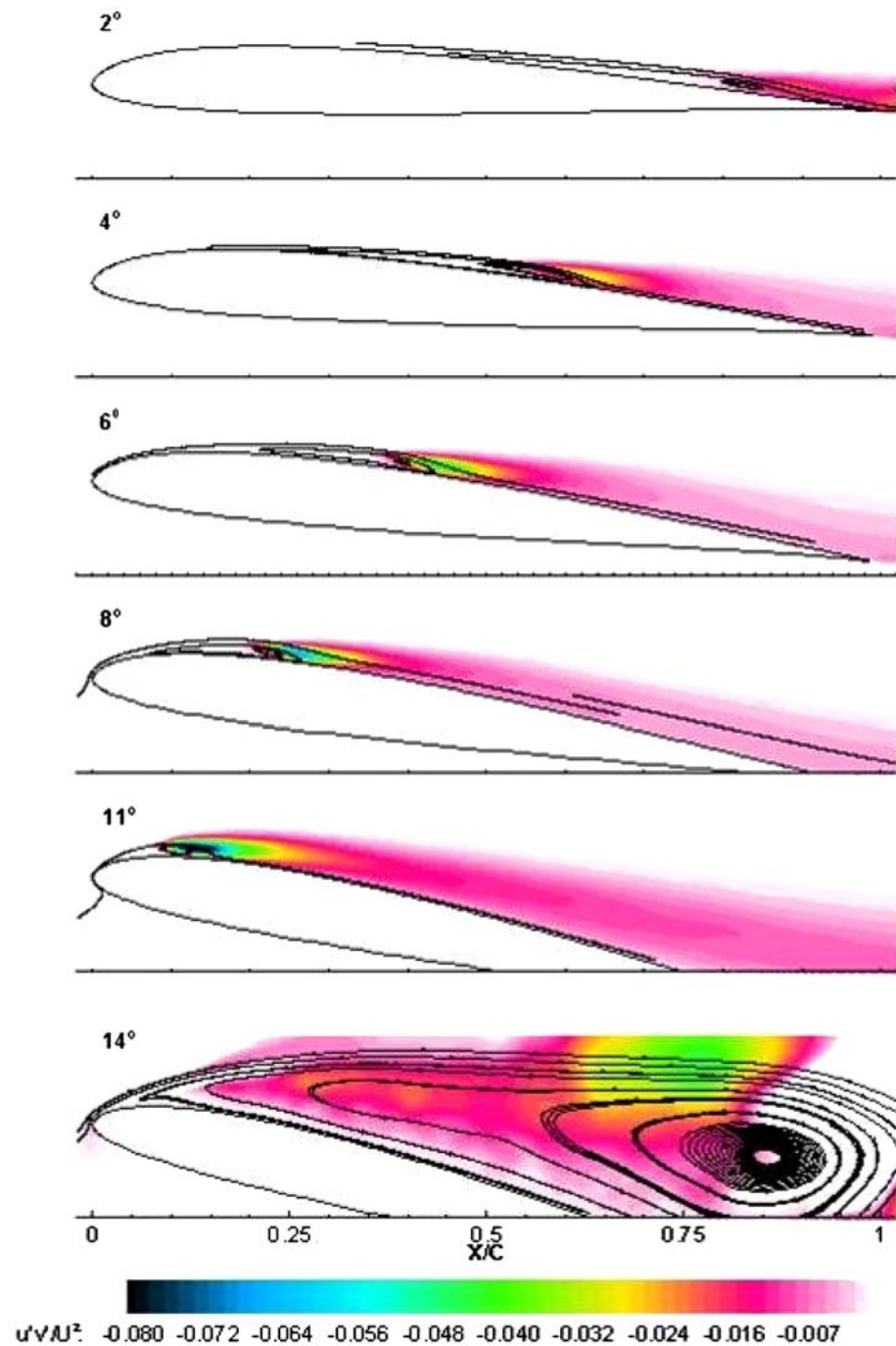
computed flow fields, which may account for differences in the LSB size. Elucidation of these effects would require additional computational and experimental studies wherein these factors could be varied in a systematic fashion. Nonetheless, given all the sources of uncertainty, the level of agreement observed is found to be encouraging. Additional comparison with experiments, including different angles of attack and aerodynamic loads is provided in Galbraith and Visbal (2008).

The present high-fidelity simulations permit a characterization of the complex three-dimensional flow structure which is more difficult to obtain from experimental measurements. The evolution of the computed three-dimensional instantaneous flow structure with increasing angle of attack
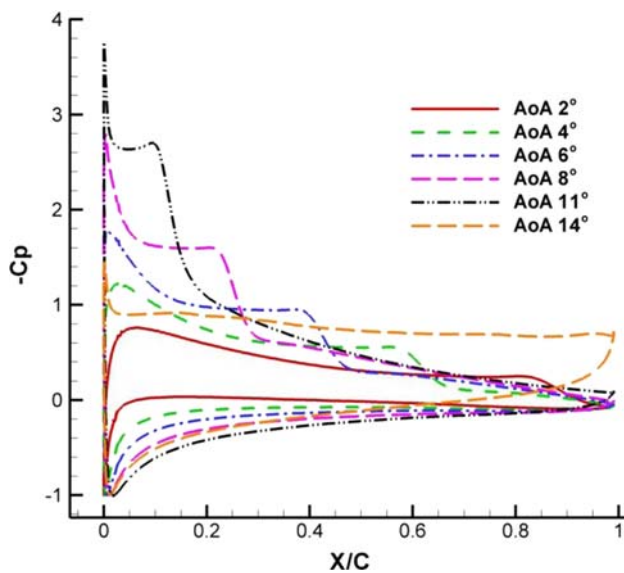
Fig. 2 Effect of angle of attack on mean surface pressure distribution, $Re_c = 6 \times 10^4$

Table 1 Effect of angle of attack on computed LSB properties

α (degrees)	Separation (x_s/c)	Reattachment (x_r/c)	Max bubble height (h_b/c)
2	0.45	0.92	0.036
4	0.23	0.65	0.030
6	0.11	0.45	0.028
8	0.04	0.28	0.027
11	0.007	0.16	0.025
14	0.01	–	–

$Re_c = 6 \times 10^4$

is shown in Fig. 4. This figure displays iso-surfaces of the Q-criterion (Dubeif and Delcayre 2000) which provides a means of visualizing vortical structures. At the lowest incidence ($\alpha = 2°$), the breakdown of the separated shear layer begins to emerge just upstream of the trailing edge. Significant changes occur with a small increase in angle of attack to $\alpha = 4°$. Coherent vortices form in the separated shear layer and rapidly breakdown due to spanwise instability effects. Nonetheless, the original coherent spanwise structures, surrounded by fine-scale features, are still discernable. With further increase in angle of attack (up to $\alpha = 11°$), the shear-layer vortices form closer to the leading edge, and the viscous flow region above the airfoil is characterized by progressively less coherent fine-scale features associated with the earlier transition to turbulence. Finally, for $\alpha = 14°$, the shear layer fails to reattach following separation from the leading edge and large scale vortex shedding ensues. These results demonstrate that the

ILES approach is capable of capturing without change in parameters the entire process of laminar boundary layer separation, shear-layer transition, reattachment of the LSB, and eventually the passage into full airfoil stall.

The present high-fidelity 3-D simulations indicate that the dynamics of the flow remains qualitatively unchanged prior to stall ($2° < \alpha < 11°$). In all cases, the flow stays fairly aligned with the airfoil surface, and transition takes place through the formation of a closed separation bubble in a time-averaged interpretation. In an unsteady sense, coherent vortices form in the separated shear layer and exhibit spanwise instabilities and subsequent breakdown into fine-scale turbulent structures. High magnitudes of Reynolds stresses are generated which promote reattachment to the surface. This process becomes more abrupt as the angle of attack and the corresponding adverse pressure gradient increases, resulting in a shorter mean LSB. This consistent flow evolution for a stationary airfoil prior to stall therefore appears amenable to being captured by 2-D Reynolds-averaged simulations employing simplified transition models (Shyy 2008; Radespiel et al. 2006; Yuan et al. 2005). Significant challenges however are anticipated when using those approaches for stalled flows or for highly maneuvering and flexible airfoils involving the generation of dynamic-stall-like vortices.

3.2 Effect of Reynolds number

In order to explore the effect of Reynolds number on the transition process, several computations were performed for a fixed angle of attack ($\alpha = 8°$) over the Reynolds number range $10^4 < Re_c < 9 \times 10^4$. Results for the time-averaged flow fields are shown in Figs. 5, 6, as well as in Table 3.

For the lowest Reynolds number considered ($Re_c = 10^4$), the time-averaged flow exhibits a large recirculation zone above the airfoil. The corresponding surface pressure distribution displays a very weak suction peak and a fairly flat distribution over the suction side. Only small values of Reynolds stress are observed near the trailing-edge region. For $Re_c = 3 \times 10^4$, a better defined LSB begins to emerge, and there is a significant increase in the magnitude of the Reynolds stress. However, the LSB is still fairly large and produces significant boundary-layer displacement. The corresponding C_p distribution shows a stronger suction peak followed by a plateau and a mild recovery. As Reynolds number increases further, the separation location remains effectively unchanged while the LSB shrinks considerably in size. This is also accompanied by a more effective recovery in the surface pressure distribution. The variation of the mean drag with Reynolds number for a fixed angle of attack is given in Table 3. It is apparent that with decreasing Re_c there is a significant

Fig. 3 Comparison of computed and experimental mean streamline pattern, Reynolds stress and velocity profiles for $Re_c = 6 \times 10^4$ and $\alpha = 4°$

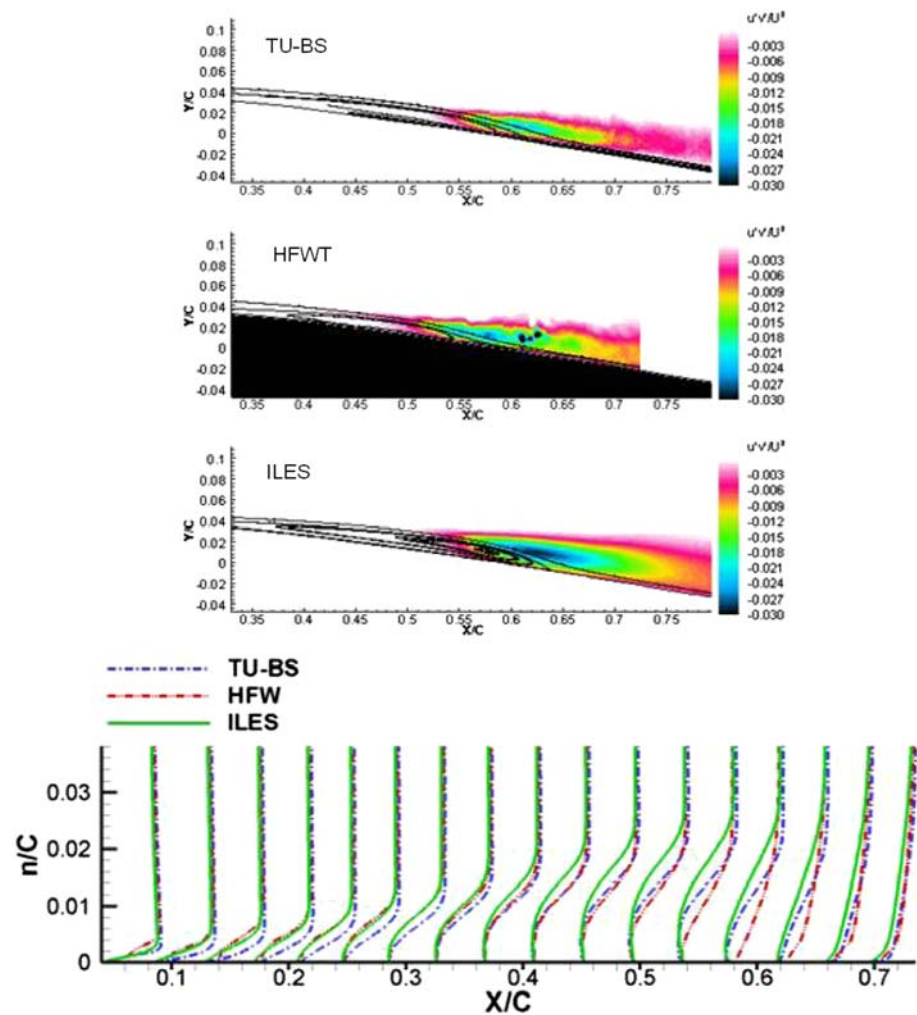**Table 2** Comparison of experimental and computed LSB properties

Data set	Freestream turbulence (%)	Separation (x_s/c)	Reattachment (x_r/c)	Max bubble height (h_b/c)
TU-BS	0.08	0.30	0.62	0.028
HFWT	0.1	0.18	0.58	0.029
ILES	0	0.23	0.65	0.030

$\alpha = 4°$, $Re_c = 6 \times 10^4$

increase in the mean drag coefficient. This reduction in aerodynamic performance is a direct consequence of the significant vertical displacement effect created by the larger LSB at lower Reynolds number (Fig. 5).

The evolution of the instantaneous three-dimensional flow structure is shown in Fig. 7, using again an iso-surface of the Q-criterion. For $Re_c > 3 \times 10^4$, the process of boundary layer transition is clearly observed. In addition, finer scale turbulent flow features are generated with increasing Reynolds number. At the lowest Reynolds number considered ($Re_c = 10^4$), shear layer transition does

not occur above the airfoil. Instead, the flow is characterized by the formation of large-scale coherent vortices which are shed from the leading edge and which only exhibit mild spanwise instabilities in the aft-region of the airfoil. It is expected that the effect of Reynolds number on the transition process depends also on angle of attack. Additional results showing Reynolds number effects for $\alpha = 4°$ and $\alpha = 14°$ are presented in Galbraith (2009) and Visbal (2009). At the lower incidence the flow failed to transition for $Re_c = 10^4$. In the stalled regime ($\alpha = 14°$), transition of the separated shear layer takes place in the aft-portion of the airfoil for $Re_c = 10^4$.

4 Transitional flow over plunging SD7003 airfoil

In this section, the influence of a prescribed motion on the transitional low-Reynolds-number airfoil flow is examined. Computations were performed for a plunging SD7003 airfoil section for which recent PIV measurements (McGowan
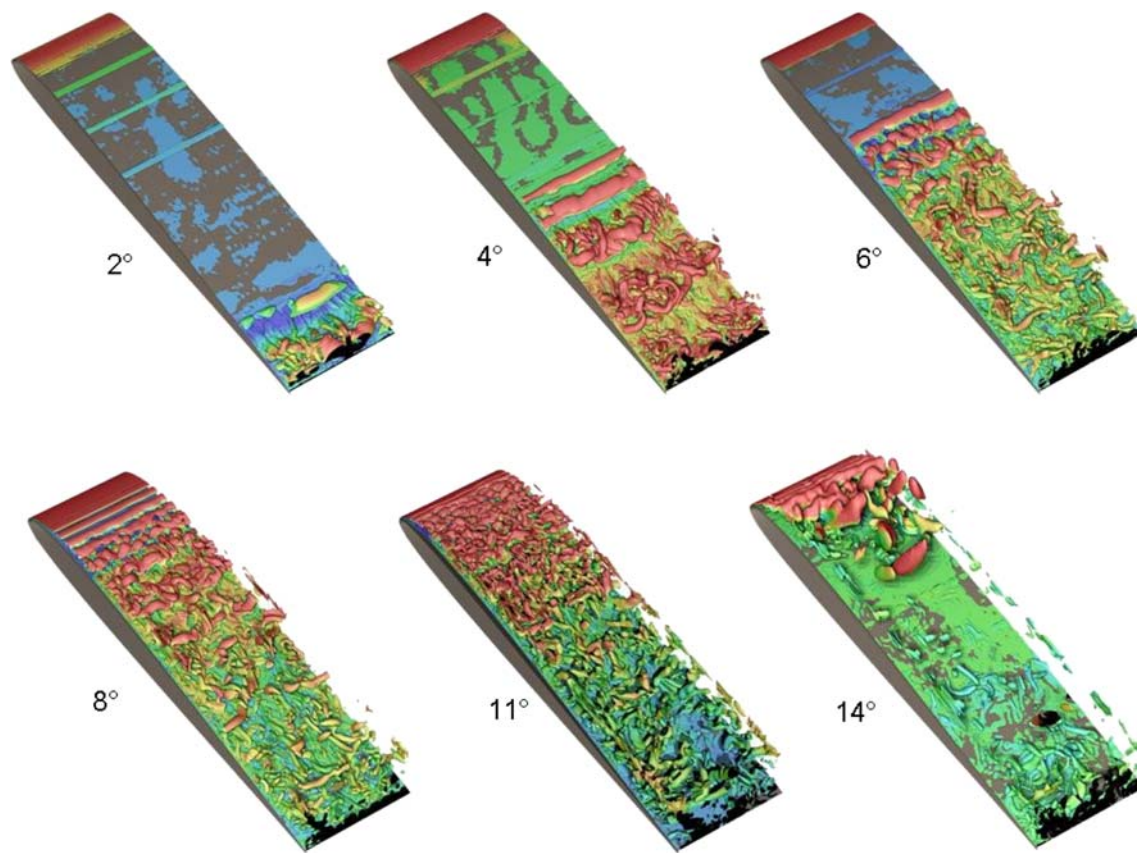
**Fig. 4** Evolution of instantaneous three-dimensional flow structure with angle of attack, $Re_c = 6 \times 10^4$

et al. 2008) have been conducted. The airfoil is set at a static angle of attack $\alpha_o = 4°$, and the reduced frequency and plunging amplitude are $k = \pi fc/U_\infty = 3.93$ and $h/c = 0.05$, respectively. These motion parameters result in a maximum excursion in induced angle of attack of $21.5°$ which should promote leading-edge separation and the generation of dynamic-stall-like vortices. Two different Reynolds numbers ($Re_c = 10^4$ and 4×10^4) are considered in order to explore the impact of transition on the flow structure over the plunging airfoil.

Details of the computational mesh generated around the SD7003 airfoil are described elsewhere (Visbal 2009). Grid points were concentrated near the airfoil in order to capture the transition process. Therefore, description of the wake is limited to the region just downstream of the airfoil trailing edge (up to $x/c = 2.0$). Study of the downstream evolution of the wake far away from the airfoil is not considered since a larger grid would be needed. Both 2-D and 3-D simulations were performed in order to explore the suitability of the much more efficient 2-D approach for low-Reynolds-number applications, as well as to compare with previous computations (McGowan et al. 2008). For the 3-D calculations, the flows were assumed to be periodic in the

spanwise direction with an extent $s/c = 0.2$. This value of s was selected based on a previous investigation of the effect of spanwise extent on the transitional flow past the same airfoil geometry at fixed angle of attack (Galbraith and Visbal 2008).

Comparison of the instantaneous spanwise vorticity component obtained from both 2-D and 3-D computations is shown at a given phase of the plunging motion in Fig. 8. For $Re_c = 10^4$, the 2-D and 3-D results are in close agreement with each other over a significant portion of the airfoil. Some discrepancies exist in the aft-portion near the trailing edge, as well as in the near wake due to incipient 3-D effects. However, the leading-edge vortex formation in particular exhibits a two dimensional character. This behavior appears to be consistent with the previous stationary airfoil (Sect. 3) for which transition was not observed at this low Reynolds number. As the Reynolds number is increased to 4×10^4, significant differences emerge between 2-D and 3-D results. The coherent vortices observed in the 2-D simulations breakdown in the spanwise direction, as described in more detail later. Given the importance of spanwise effects, only results from 3-D computations are discussed below.

Springer

Fig. 5 Effect of Reynolds number on time-averaged flow structure, $\alpha = 8°$
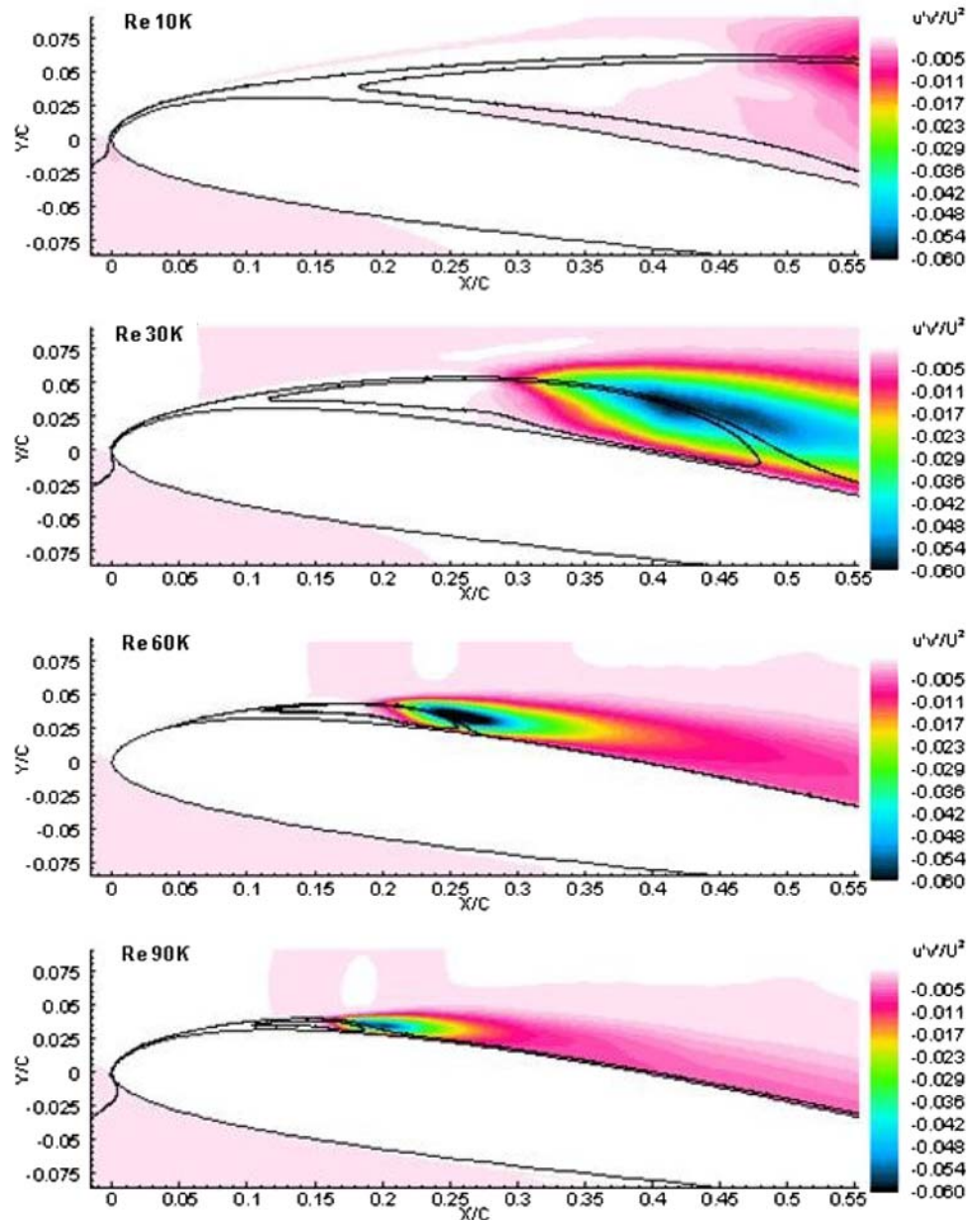
The computed instantaneous flow structure over the plunging airfoil for $Re_c = 10^4$ is shown in Fig. 9. The selected motion phases correspond to the positions of maximum upward displacement ($\Phi = 0$), maximum downward velocity ($\Phi = 1/4$), maximum downward displacement ($\Phi = 1/2$) and maximum upward velocity ($\Phi = 3/4$). Although not included here, at this lower Reynolds number, the overall instantaneous and phase-averaged flow structures are found to be in reasonable agreement with each other due to the limited impact of transition (Visbal 2009). A fairly good comparison between experimental and phase-averaged vorticity is also shown in Visbal (2009).

Due to the large angle attack induced by the plunging motion during the downstroke, leading-edge separation occurs on the upper surface of the airfoil, and coherent dynamic-stall-like vortices are generated. Two distinct leading-edge vortices (denoted as '1' and '2' in Fig. 9c) are formed by the time the airfoil reaches its bottom dead center. During the upstroke, these vortices propagate close to the airfoil surface thereby precluding massive stall for this high value of reduced frequency. Given the short period of the motion ($T = \pi/k = 0.8$), the dynamic stall vortices emerge before the pair of vortices generated in the previous cycle (denoted as '3' and '4' in Fig. 9d) have reached the airfoil trailing edge. In addition to the primary
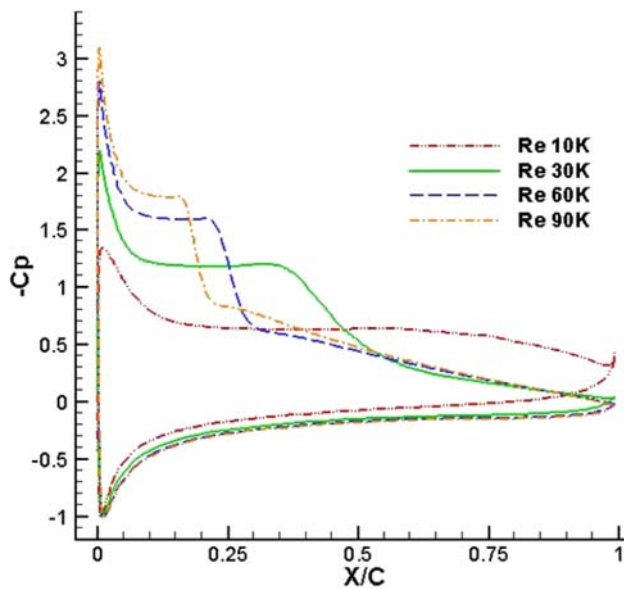
🖄 Springer

Fig. 6 Effect of Reynolds number on mean surface pressure distribution, $\alpha = 8°$

Table 3 Effect of Reynolds number on computed LSB propreties and mean drag coefficient

Re_c	Separation (x_s/c)	Reattachment (x_r/c)	Max bubble height (h_b/c)	Mean drag $(C_{D_{\text{mean}}})$
1×10^4	0.09	0.98	0.217	0.082
3×10^4	0.05	0.53	0.073	0.070
6×10^4	0.04	0.28	0.027	0.043
9×10^4	0.04	0.20	0.014	0.035

$\alpha = 8°$

leading-edge vortical structures, another distinct feature is the ejection of vorticity of the opposite sign due to the ensuing vortex surface interaction. This ejected vorticity is quite prominent between the two primary dynamic-stall vortices (Fig. 9d), and eventually surrounds completely the leading vortex (denoted as '1'). Further downstream, this secondary vorticity becomes less apparent due to spanwise instability effects, as discussed below. Separation and formation of a single dynamic-stall vortex is also observed on the airfoil lower surface (Fig. 9b) as a result of the large negative angle of attack induced during the upstroke.

The present implicit large-eddy simulations permit a detailed description of the 3-D instantaneous flow structure which complements experimental planar observations. The overall instantaneous 3-D flow features for $Re_c = 10^4$ are displayed for several phases in Fig. 10. These plots show an iso-surface of vorticity magnitude colored by density in order to enhance contrast. At all phases of the plunging motion shown, one can observe coherent spanwise vortical

structures or rollers which exhibit a fairly 2-D character. These vortices are surrounded by complex 3-D flow features resulting from spanwise instabilities. In particular, the dynamic stall vortex forming near the leading edge retains its spanwise coherence; however, the vorticity ejected from the airfoil surface (as a result of the strong vortex–surface interaction) rapidly breakdowns giving rise to the appearance of longitudinal vortical structures. Therefore, for this high reduced frequency and low Reynolds number, transitional effects over the airfoil appear to be minor, and are associated with the ejected secondary vorticity. However, as discussed next, this situation changes significantly with increasing Reynolds number.

Results for $Re_c = 4 \times 10^4$ are considered next. Figure 11 displays a comparison of the experimental and computed phase-averaged streamwise velocity and spanwise vorticity contours at the end of the upstroke. The computed results are found to be in reasonable qualitative agreement with the experimental measurements. A more quantitative comparison is shown in Fig. 12 in terms of the streamwise velocity profiles in the near wake at $x/c = 1.5$. The agreement between the measured and computed profiles is in general quite good. The velocity profile corresponding to the phase of maximum vertical displacement ($\Phi = 0$) exhibits a well-defined jet character. This jet-like behavior is consistent with the fact that the trailing-edge vortex shed from the airfoil lower surface is above the vortex shed from the upper surface boundary layer (see Fig. 11c, d). As it will be discussed later, this inverted vortex street results in a net mean thrust.

The computed instantaneous and phased-averaged spanwise vorticity fields are shown in Fig. 13. Significant differences are observed between the instantaneous and phased-averaged representations which reflect the fully 3-D transitional nature of the flow. The instantaneous vorticity exhibits fine-scale flow features within the dynamic stall vortices, as well as in the near wake. These features are essentially eliminated in the phase-averaging process. Increasing the Reynolds number has clearly modified the details of the phase-averaged vortical structure emerging from the unsteady separation process near the airfoil leading edge. As discussed earlier, for $Re_c = 10^4$ (Fig. 9c, d), the leading-edge vortex system exhibited a pair of dynamic-stall-like vortices which retained their identity as they propagated downstream in the absence of significant spanwise transitional effects. By contrast, for $Re_c = 4 \times 10^4$ (Fig. 13), a single and more diffused leading-edge vortex is observed in the phased-averaged representation.

The computed instantaneous 3-D flow structure above the plunging airfoil for $Re_c = 4 \times 10^4$ is displayed in Fig. 14. The most prominent overall flow features are the leading-edge vortices and their breakdown into fine-scale turbulence due to spanwise instability effects. At the end of
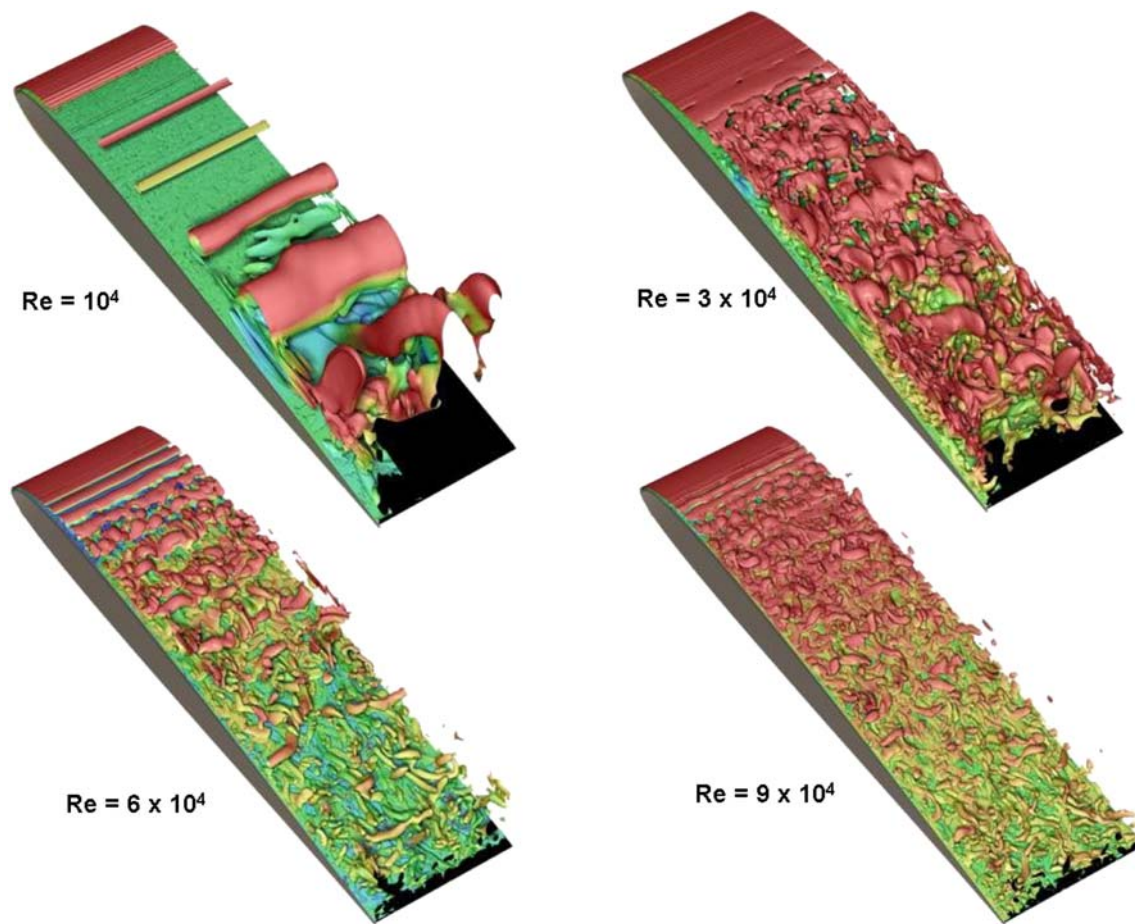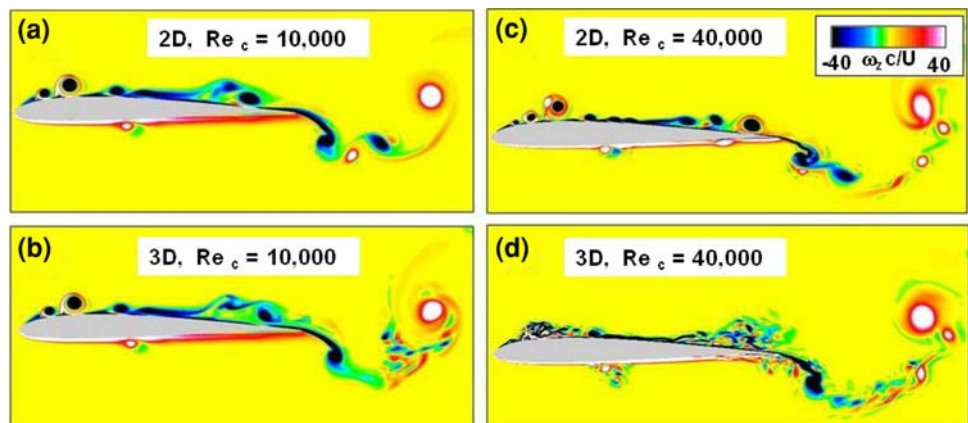
Fig. 7 Effect of Reynolds number on three-dimensional instantaneous flow structure, $\alpha = 8°$

Fig. 8 Comparison of instantaneous spanwise vorticity for 2-D and 3-D plunging airfoil simulations

the upstroke ($\Phi = 0$), the boundary layer near the leading edge remains laminar and attached to the airfoil surface. By the time the airfoil has reached its maximum downward velocity ($\Phi = 1/4$), a small region of laminar separation has emerged near the leading edge. Between $\Phi = 1/4$ and $\Phi = 1/2$, this separation region evolves into a coherent dynamic-stall-like vortex which subsequently breakdowns into fine-scale structures. This transitional leading-edge

vortex propagates downstream close to the airfoil surface, as seen in Fig. 13. Given the relatively high value of reduced frequency, the dynamic-stall-like vortex generated in the previous cycle (denoted as V_1 in Fig. 14c) has not reached the airfoil trailing edge before a new leading-edge vortex (V_2) is generated.

The transition of the dynamic stall vortex near the leading edge is described in detail in Visbal (2009). This

Fig. 9 Instantaneous spanwise vorticity at selected phases of the plunging motion for $Re_c = 10^4$
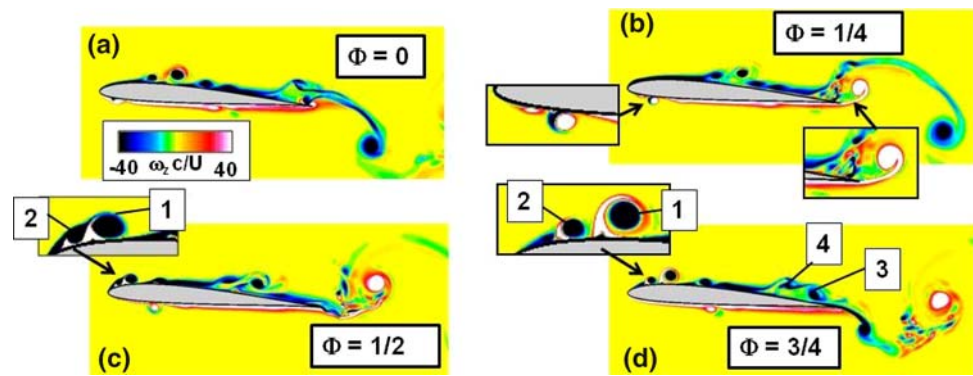
Fig. 10 Iso-surface of instantaneous vorticity magnitude at selected phases of the plunging motion for $Re_c = 10^4$
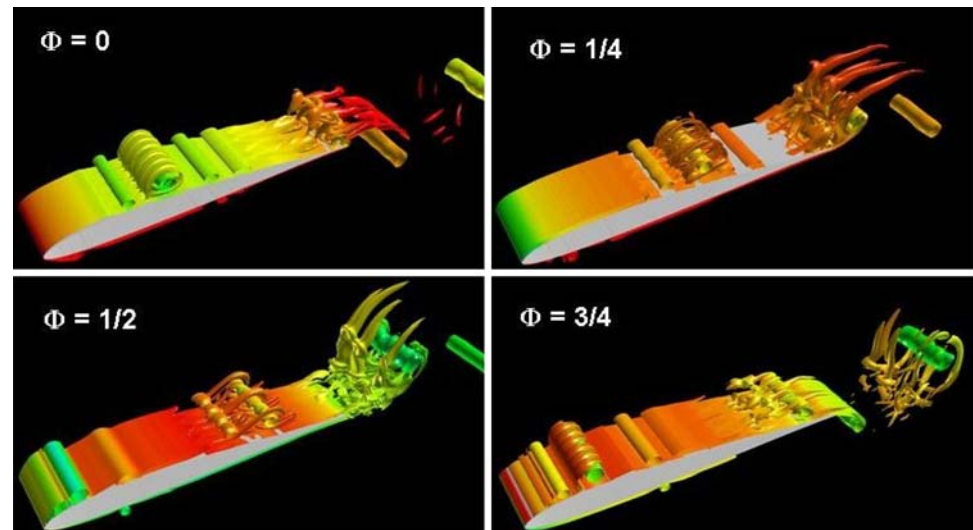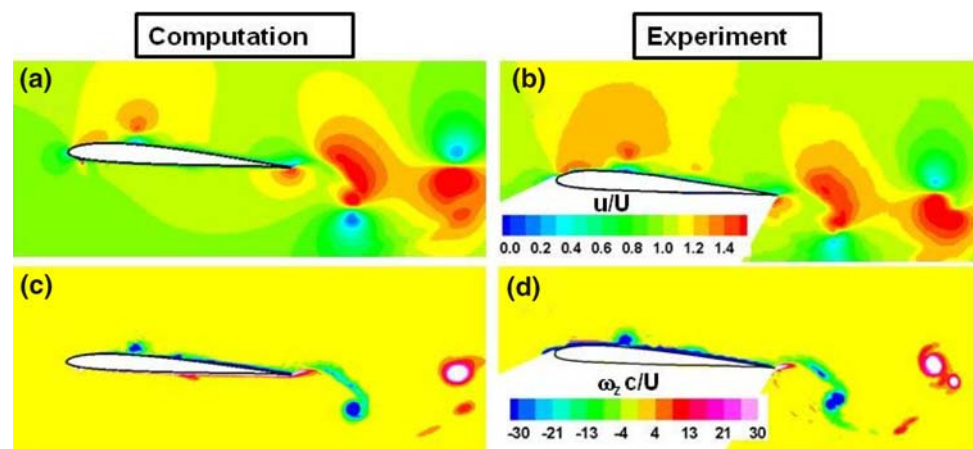

Fig. 11 Comparison of computed and experimental phased-averaged streamwise velocity (**a**, **b**) and spanwise vorticity (**c**, **d**) at the end of the upstroke for $Re_c = 4 \times 10^4$

transition process is found to be rather abrupt and takes place over a short non-dimensional time interval of order $\Delta t U_\infty / c \leq 0.04$. This represents a fast onset compared to either the plunging motion or the vortex convection time scales. If remains to be seen whether this process can be duplicated by standard Reynolds-averaged eddy-viscosity models which rely on dissipation-like terms. In addition,

the mixed laminar-transitional character of this highly unsteady flow is quite apparent. For instance, the vortex structure of Fig. 14c displays an extensive region of fairly laminar flow between the two transitional leading-edge vortices generated in consecutive cycles of the plunging motion. This mixed flow structure, although amenable to simulation with the present high-fidelity ILES approach,

Fig. 12 Comparison of computed and experimental phased-averaged streamwise velocity profiles in the near wake ($x/c = 1.5$) of the plunging airfoil for $Re_c = 4 \times 10^4$
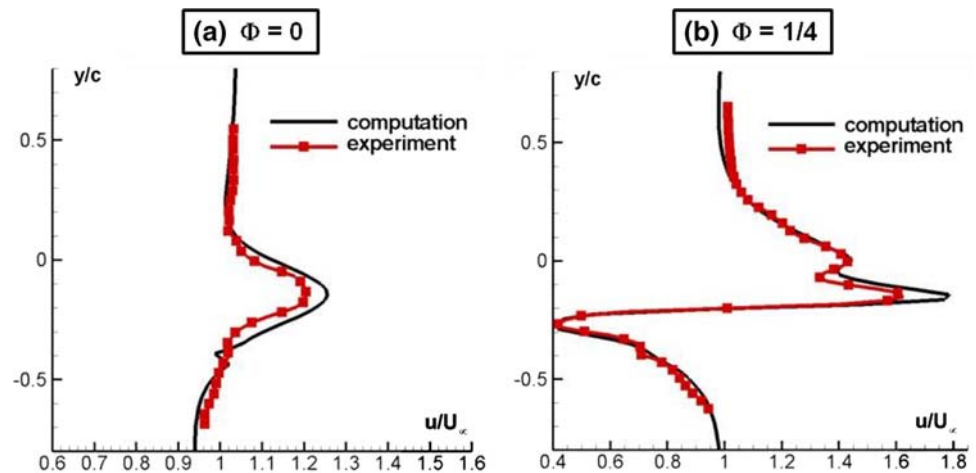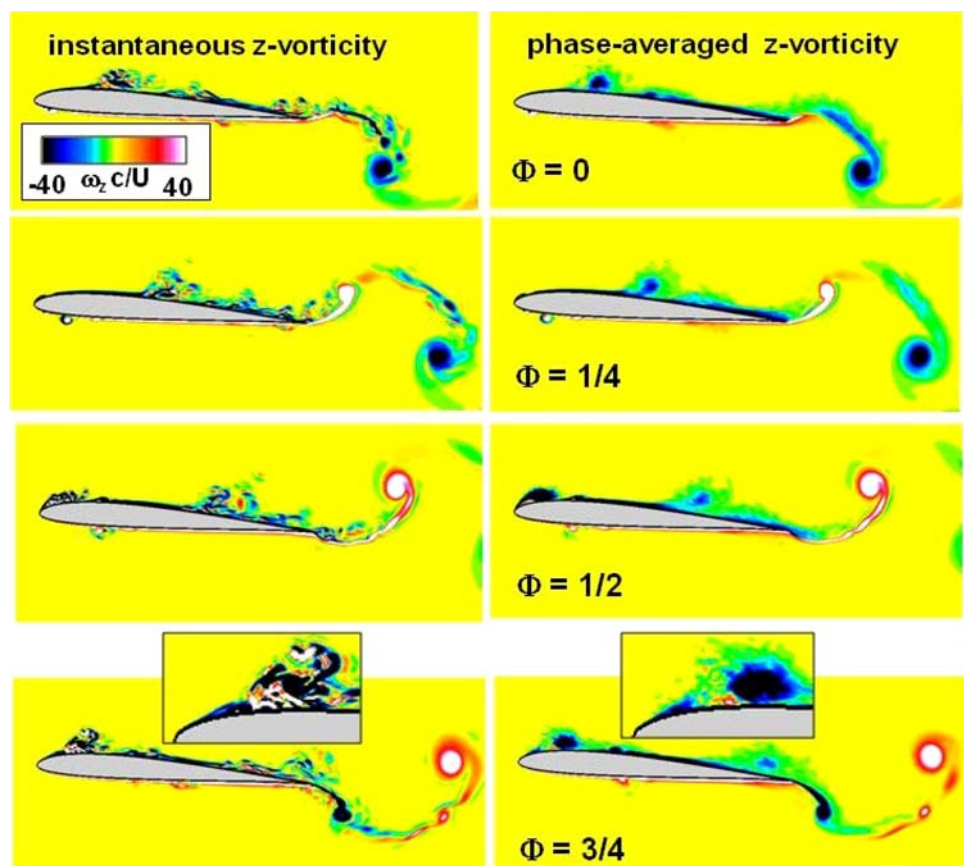

Fig. 13 Comparison of computed instantaneous and phased-averaged spanwise vorticity at selected phases of the plunging motion for $Re_c = 4 \times 10^4$

will remain a significant challenge for more efficient Reynolds-averaged methods incorporating simplified transition models.

The time histories of the lift coefficient for both Reynolds numbers are shown in Fig. 15a. Clearly, C_L appears to be essentially independent of Reynolds number and of the 3-D transitional aspects of the flow field. The insensitivity of the aerodynamic lift is due to the fact that at this high value of reduced frequency, C_L is dominated by the acceleration of the airfoil which scales with k^2. Indeed, the

computed lift is found to be in close agreement with the prediction given by the inviscid theory (Fung 1993) (Fig. 15b) which in turn is shown to be dominated by non-circulatory effects. The computed mean drag coefficients for $Re_c = 10^4$ and $Re_c = 4 \times 10^4$ were found to be -0.055 and -0.083, respectively, where negative C_D values correspond to net thrust on the airfoil. As it is perhaps to be expected, the drag coefficient shows a significant dependence on Reynolds number and on the transitional aspects of the flow.

Fig. 14 Iso-surface of instantaneous vorticity magnitude showing flow structure above plunging airfoil at selected phases of the plunging motion for $Re_c = 4 \times 10^4$
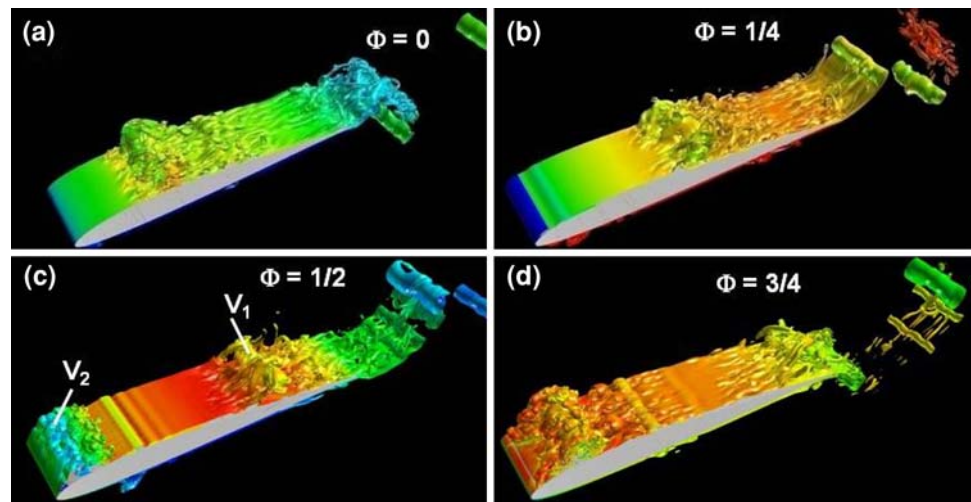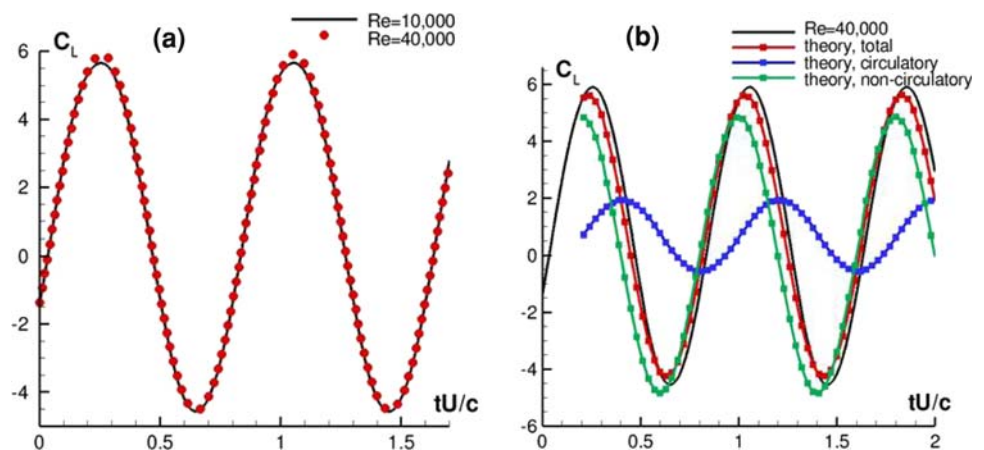

Fig. 15 Computed lift coefficient histories for plunging airfoil

5 Flexible membrane airfoil

In this section, the impact of fluid–structure interaction on the low-Reynolds-number flow past a flexible airfoil is investigated. The membrane airfoil configuration considered is based on the experimental model of Rojratsirikul, Wang, and Gursul (Rojratsirikul et al. 2008). In these experiments, the membrane wing consists of a thin latex sheet stretched between two small, aerodynamically-shaped, rigid mounts. The sheet is glued to the mounts resulting in pinned boundary conditions for the flexible membrane. Experimental observations (Rojratsirikul et al. 2008) indicate that the membrane deformation is essentially uniform in the spanwise direction. This observation justifies the initial assumption of 2-D deformation, at least for low Reynolds number simulations.

For the present computations, a freestream Mach number $M_\infty = 0.05$ is prescribed in order to approach the incompressible situation. Unless otherwise noted, the results presented are for a Reynolds number based on airfoil chord of $Re_c = 2{,}500$. The static angle of attack ranged

from $\alpha = 4°$ to $\alpha = 20°$. The membrane structural parameters in Eq. 2 are specified as follows: mass ratio, $\rho_s h = 0.589$, membrane rigidity, $Eh = 50$, no structural damping, $C_d = 0$, and no membrane pretension, $\delta_o = 0$. To explore the impact of transition an additional computation at a higher Reynolds number ($Re_c = 4.85 \times 10^4$), and with structural parameters $Eh = 14.48$ and $\rho_s h = 1.2$ is also presented. Further simulations for higher Reynolds numbers and for other values of the structural parameters are described in Gordnier (2008) and Gordnier and Attar (2009) wherein additional details of the computations can also be found.

The evolution of the time-averaged flow structure with increasing angle of attack is shown in Figs. 16, 17, and 18 in terms of the mean vorticity and streamline patterns, the membrane shape and pressure distributions, as well as the mean aerodynamic lift coefficient. The most obvious effect of flexibility is the development of significant camber in the mean shape of the membrane due to the differences in pressure between the upper and lower sides of the airfoil. The maximum deflection (Fig. 17a) grows over the

Springer

14
Approved for public release; distribution unlimited

Fig. 16 Mean vorticity and streamline patterns for membrane airfoil at selected angles of attack: **a, f** $\alpha = 4°$; **b, g** $\alpha = 8°$; **c, h** $\alpha = 12°$; (**d, i**) $\alpha = 16°$; and (**e, j**) $\alpha = 20°$
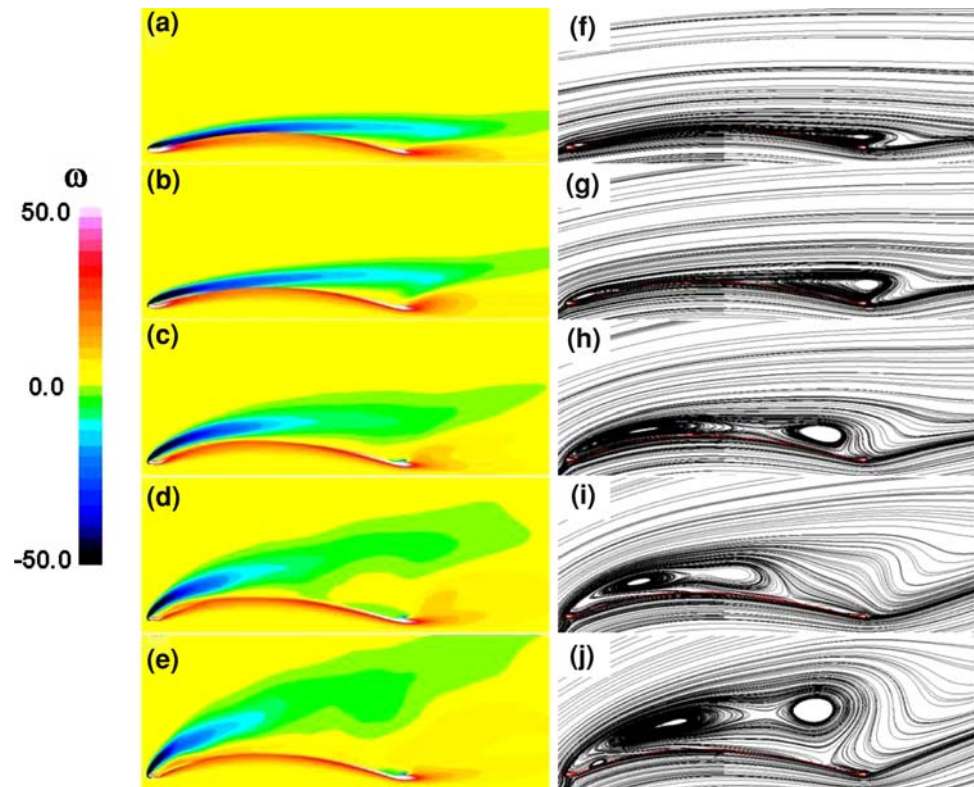
incidence range considered from $z_{max}/c = 0.0724$ at $\alpha = 4°$ to $z_{max}/c = 0.0899$ at $\alpha = 20°$. For $\alpha = 4°$ the membrane shape is nearly symmetric. However, it becomes progressively more asymmetric with increasing incidence. For $\alpha = 16°$, the point of maximum deflection reaches $x/c = 0.426$ before it starts moving back downstream with further increase in angle of attack.

The impact of increasing angle of attack (and correspondingly mean camber) on the overall mean flowfield is shown in Fig. 16. At $\alpha = 4°$, the flow detaches at $x/c = 0.738$ resulting in a narrow separation bubble which extends to the trailing edge (Fig. 16f). A very small separation bubble is present near the leading edge associated with the rigid membrane mount. It should be noted that separation was always found to occur at the rigid mount. This fact suggests that how the underlying support structure for a membrane is designed may have direct influence on the flexible airfoil performance. As the angle of attack is raised to $\alpha = 8°$, the downstream separation point moves forward to $x = 0.57$, and the normal extent of the separation bubble increases. The leading-edge separation bubble also increases in size with attachment occurring at $x = 0.161$. By $\alpha = 12°$ the two separation zones have merged creating one large separation region that is narrow in vertical extent and covers nearly the full length of the airfoil. At $\alpha = 16°$, the separation zone has shrunk with attachment at $x = 0.774$, but the normal extent of the separated region has grown. Finally, by $\alpha = 20°$, a

massively separated flow region exists over the airfoil. A small secondary separation zone is also observed near the leading edge of the membrane.

The corresponding evolution of the mean vorticity field is shown in Fig. 16a–e. At the lowest angle of attack (Fig. 16a), the shear layer separates from the upstream mount but rapidly attaches to the membrane airfoil. It subsequently departs from the membrane surface downstream at the previously noted separation location. By $\alpha = 12°$ (Fig. 16c), the shear layer separates from the upstream mount and fails to reattach to the membrane surface. A significant thickening of the shear layer is also observed. At the higher angles of attack, the departure angle of the shear layer from the leading edge mount grows and the shear layer moves increasingly away from the membrane. At $\alpha = 20°$ (Fig. 16e), a small region of vorticity of the opposite sign is located under the shear layer near the leading edge associated with the development of secondary separation.

The resulting mean surface pressure distributions on the membrane are plotted in Fig. 17b. As the incidence angle increases, a well-defined suction peak develops on the upper surface in the leading edge region. On the lower surface, the pressure progressively increases with angle of attack.

Shown in Fig. 18 is a comparison of the mean lift coefficient for the flexible membrane airfoil, as well as for a rigid flat airfoil. The C_L distribution for a symmetric

Fig. 17 Mean membrane deflection (**a**) and surface pressure coefficient (**b**) for various angles of attack
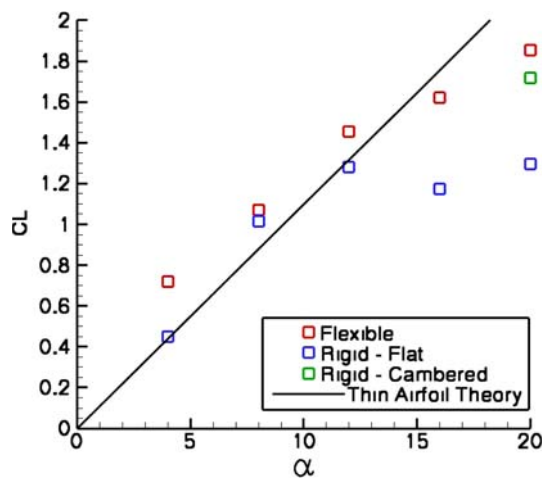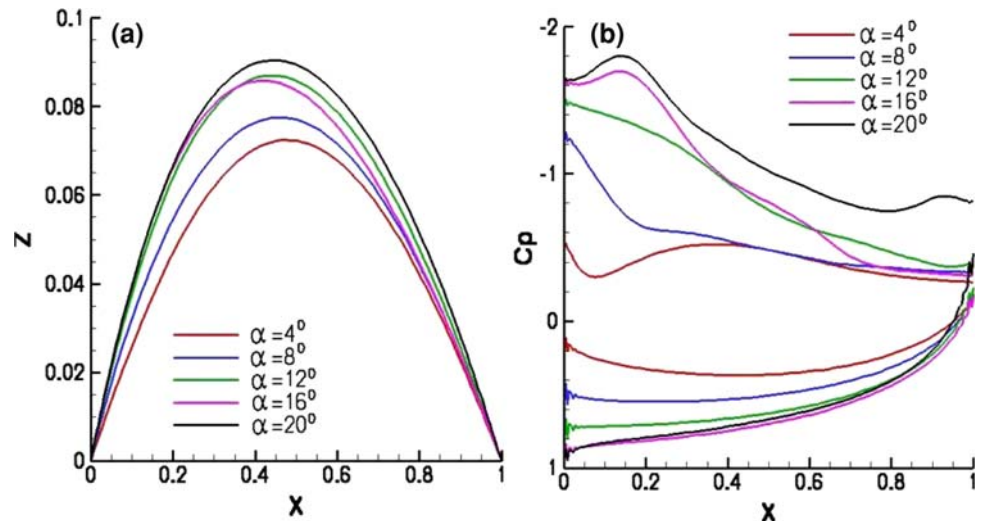

Fig. 18 Comparison of mean lift coefficient for flexible membrane and for rigid symmetric and cambered wing configurations

airfoil based on thin-airfoil theory is also shown for reference purposes. The rigid airfoil lift coefficient increases approximately in a linear fashion with a slope which is close to the theoretical value. A maximum C_L is achieved for $\alpha = 12°$. Beyond this angle of attack, the lift distribution displays the characteristics of a stalled flow. The flexible membrane airfoil exhibits a lift variation which differs significantly from its rigid counterpart. If one extrapolates the lift coefficient to zero incidence, a significant lift is achieved due to the camber effect induced by flexibility. When the angle of attack is increased up to $\alpha = 12°$, C_L increases in an approximate linear fashion albeit with a reduced slope relative to either the rigid case or the theoretical distribution. For higher incidence ($12° < \alpha < 20°$), the flexible airfoil lift coefficient continues to rise, although there is a further reduction in the lift-curve slope. Therefore, at high angles of attack, airfoil

flexibility results in substantial lift enhancement relative to the rigid case. For the range of α considered, there appears to be no evidence of stall for the membrane airfoil, at least in terms of the aerodynamic lift coefficient. Lift enhancement due to wing flexibility at high angles of attack has also been demonstrated in wind tunnel tests by Waszak et al. (2001) and is due to both the effect of the induced mean camber, as well as the dynamic surface motion to be described next.

Instantaneous snapshots of the vorticity field (Fig. 19) illustrate the evolving unsteady flow structure with increasing angle of attack. At $\alpha = 4°$, the flow separates just past the midpoint of the airfoil. The separated shear layer does not become unstable or roll up until it passes the trailing edge and interacts with the separating flow from the lower surface. Therefore, the flow over the airfoil is predominantly steady. As the angle of attack is increased, the onset of the shear layer rollup moves progressively upstream and the flow becomes increasingly unsteady over the airfoil. Up to $\alpha = 12°$, the vortices remain close to the airfoil surface as they propagate downstream. At $\alpha = 16°$, the vortex train begins to depart from the membrane. The convecting shear-layer vortices interact with the surface boundary layer resulting in the development of secondary vortical structures, and the eventual eruption of vorticity of the opposite sign from the surface. Pairing of the shear-layer vortices is also observed in computed animations for the higher angles of incidence.

The unsteady structural response of the membrane airfoil is shown in Fig. 20. This figure displays the membrane oscillations by means of $x-t$ diagrams showing the difference between the instantaneous and mean membrane deflections. The membrane is nominally stationary at $\alpha = 4°$ since, as noted earlier, the flow is steady over the major portion of the airfoil (Fig. 19a). At $\alpha = 8.0°$, a third mode standing wave response develops with a
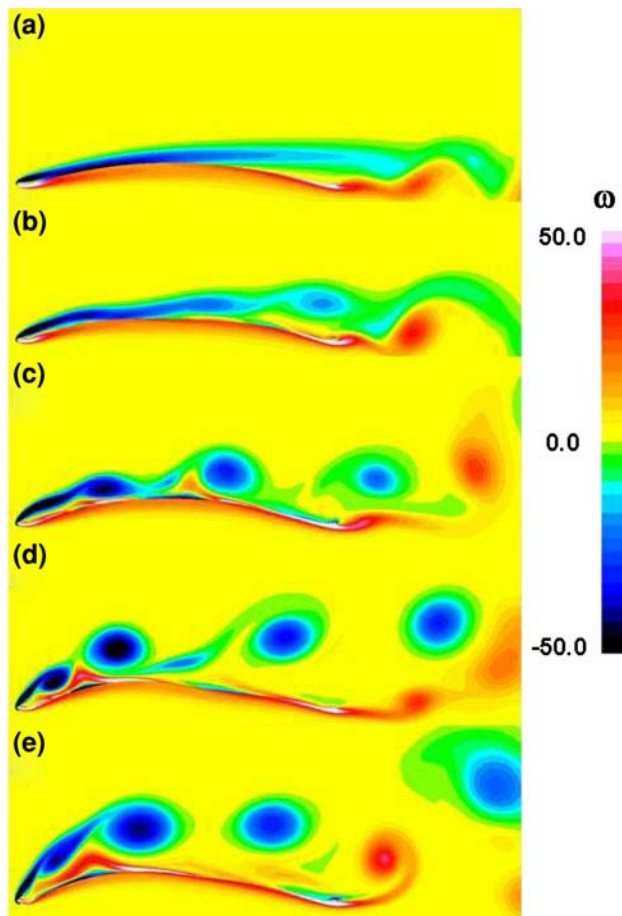
Fig. 19 Instantaneous vorticity for membrane airfoil at selected angles of attack: **a** $\alpha = 4°$, **b** $\alpha = 8°$, **c** $\alpha = 12°$, **d** $\alpha = 16°$, and **e** $\alpha = 20°$

nondimensional frequency, $St = fc/u_\infty = 1.43$. This frequency correlates within the tolerance of the Fourier analysis to the vortex shedding frequency $St \approx 1.45$ as measured at a point above the airfoil by which the shed vortices are passing. At the higher angles of attack $\alpha = 12°$ to $\alpha = 20°$ the membrane structural response exhibits a less regular behavior resulting from a combination of structural modes. Multiple frequency peaks are found in the Fourier analysis of the structural response. By $\alpha = 20°$ three peaks emerge in the spectral analysis of the structural response with the dominant frequency being $St = 0.59$. This corresponds to the computed vortex shedding frequency, $St = 0.6$, which correlates with the standard value for the wake shedding frequency when rescaled by angle of attack, $St \sin(\alpha) = 0.2$. The maximum peak-to-peak amplitude of the deflection reached values of order $0.07\,c$ which is of the same order as the maximum mean deflection (Fig. 17a). Therefore, in addition to the mean camber effect previously discussed, flexibility provides a significant forcing of the unsteady separated flow over the membrane.

In order to separate the effects of the dynamic motion of the membrane from the mean induced camber at higher angles of attack, a computation was run at $\alpha = 20°$ for a rigid cambered airfoil with its shape prescribed by the previously computed mean membrane deflection. A comparison of the mean and unsteady solutions for these two cases is shown in Fig. 21. The mean streamline patterns (Figs. 21a, b) show that the rigid airfoil flowfield exhibits a larger recirculation region, as well as a larger secondary separation bubble located further downstream on the airfoil. These significant differences between the time-averaged flows for the rigid and flexible airfoils result from a distinct change in the instantaneous vortical structure (Fig. 21c, d). The dynamic motion of the membrane excites the shear layer separating at the leading edge causing it to roll up sooner and to form a series of more coherent vortices which convect closer to the airfoil surface. The trailing edge vortex in the dynamic case is also reduced in strength and forms farther downstream and away from the airfoil. A similar comparison between a rigid cambered airfoil and a flexible membrane has been investigated experimentally by Rojratsirikul et al. (2008). Their flow visualizations (Rojratsirikul et al. 2008) also demonstrate a reduction of the separation zone due to the dynamic motion of the membrane. The overall impact of flexibility, through the combined effects of induced mean camber and dynamic motion, is a significant delay in the stall of the airfoil with a corresponding increase in lift coefficient in the post-stall region (Fig. 18). This enhanced lift arises predominantly from the effect of mean camber with additional lift enhancement resulting from the membrane motion. Further investigation of the impact of flexibility on the overall aerodynamics is warranted as it may provide a means for passively controlling the flow in order to achieve improved airfoil performance through judicious aeroelastic tailoring.

As the Reynolds number is increased from the low values considered to this point to more moderate values, the impact of transition on the flow becomes important. Figure 22 compares a laminar, 2-D simulation with a 3-D implicit LES simulation for $Re_c = 4.85 \times 10^4$ and $\alpha = 8°$. For the 2-D laminar simulation where transition of the flow cannot be captured directly (Fig. 22a), strong vortices are formed and shed from the leading edge. As these vortices convect downstream, they engender a very dynamic interaction with the flexible membrane resulting in large higher-mode fluctuations. The results of the 3-D computation using the implicit LES approach (Fig. 22b), exhibit rapid transition of the flow separating from the leading edge, and the subsequent development of large-scale coherent turbulent structures with embedded fine scale features. A more regular second-mode oscillation of the membrane results for this transitional flow. It is therefore apparent that correct prediction of the transitional behavior

Fig. 20 $x-t$ diagram of instantaneous membrane deflection for selected angles of attack: **a** $\alpha = 4°$, **b** $\alpha = 8°$, **c** $\alpha = 12°$, **d** $\alpha = 16°$, and **e** $\alpha = 20°$
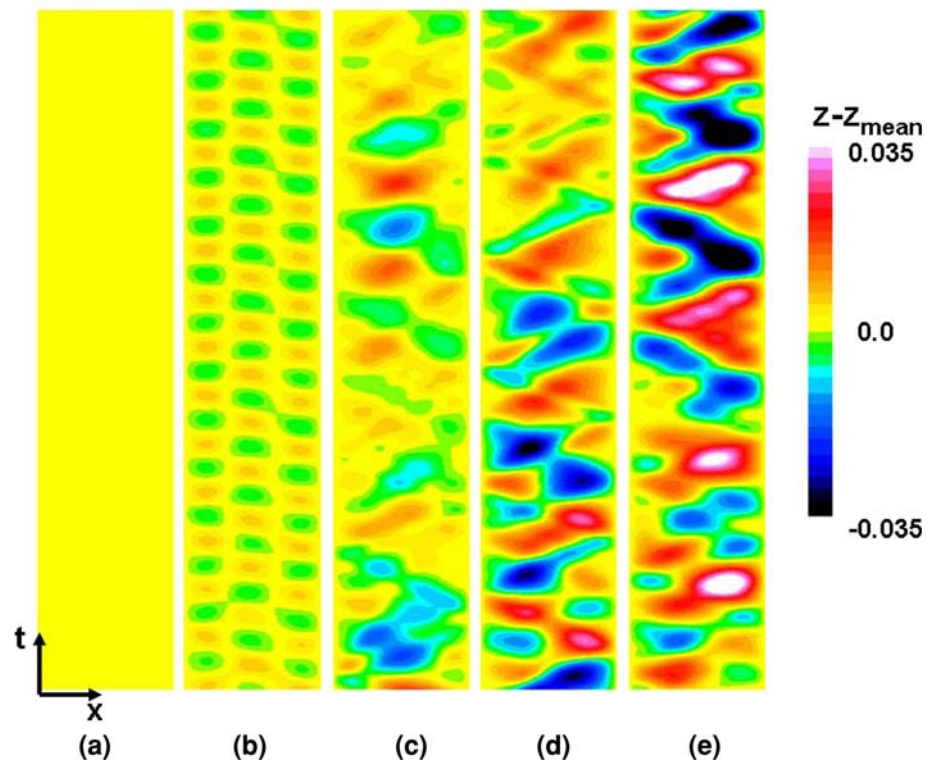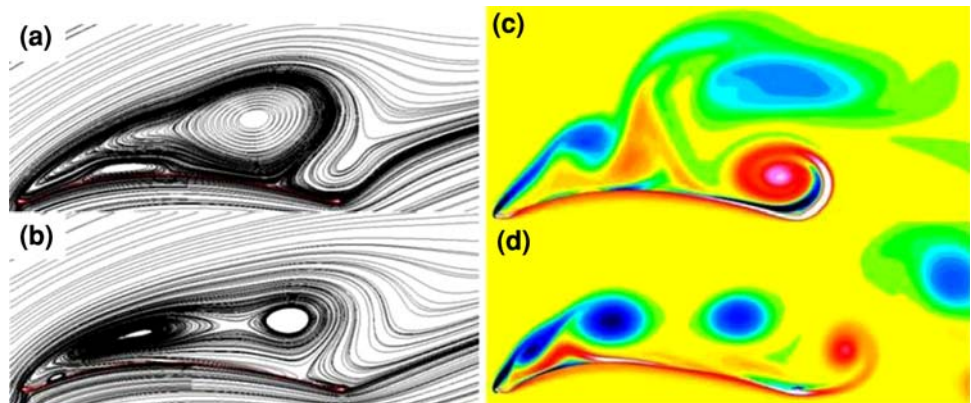

Fig. 21 Comparison of rigid cambered airfoil (**a**, **c**) and flexible membrane (**b**, **d**) flow fields for $\alpha = 20°$: **a**, **b** mean streamlines, and **c**, **d** instantaneous spanwise vorticity

is critical in order to capture the proper membrane structural response. Therefore, computational approaches that are capable of treating these unsteady, mixed transitional flows are required at these moderate Reynolds numbers. Further discussions of the ILES simulations for membrane airfoils may be found in Gordnier and Attar (2009).

6 Summary and conclusions

A high-fidelity implicit large-eddy simulation approach has been employed to investigate several aspects of the complex unsteady flow physics encountered by small-scale vehicles in low-speed flight. This regime is characterized

by highly unsteady mixed laminar-transitional-turbulent flows over moving and flexible surfaces. Three separate fluid dynamic phenomena are considered, including: laminar separation and transition over a stationary airfoil, transition effects on the dynamic stall vortex generated by a plunging airfoil, and the effect of flexibility on the flow structure above a membrane airfoil. Comparison with high-resolution PIV experiments has been provided whenever possible.

The process of boundary-layer transition over a stationary SD7003 airfoil has been examined for a range of Reynolds number ($10^4 < Re_c < 9 \times 10^4$) and angle of attack ($2° < \alpha < 14°$). Prior to stall, the flow is characterized by a separated shear layer which exhibits the

Fig. 22 Effect of transition at Reynolds number, $Re_c = 48{,}500$: **a** 2-D laminar flow simulation, **b** 3-D transitional flow simulation
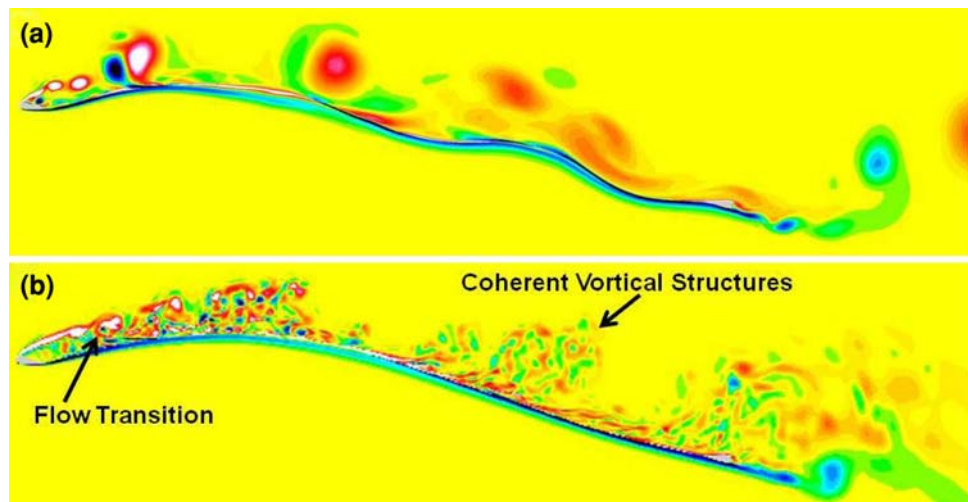
formation of spanwise coherent vortical structures. These vortices breakdown due to spanwise instability mechanisms and promote the reattachment of the boundary layer. In a time-averaged representation, a laminar separation bubble (LSB) is formed which diminishes both in streamwise and vertical extent with increasing angle of attack. At fixed incidence, decreasing Reynolds number promotes the formation of a larger LSB. By $Re_c = 10^4$, transition fails to occur over the airfoil with an accompanying significant increase in drag coefficient. The sensitivity of these transitional flows to freestream turbulence or other imposed disturbances needs to be elucidated.

The unsteady low-Reynolds-number ($Re_c = 10^4$ and 4×10^4) flow past a SD7003 airfoil plunging at a relatively high reduced frequency ($k = 3.93$) was investigated. Comparison was made with recent PIV measurements. For the parameters chosen, the large motion-induced angle of attack generates dynamic-stall-like vortices in the leading-edge region both above and underneath the airfoil. Due to the high value of k and small plunging amplitude ($h/c = 0.05$), these vortices convect downstream close to airfoil surface precluding massive stall. For $Re_c = 10^4$, the computed instantaneous and phased-averaged flow structures are in fairly good agreement with each other. This is due to the incipient process of transition which is mainly limited to the secondary vorticity ejected from the airfoil surface. When the Reynolds number is increased to 4×10^4, the dynamic-stall vortices breakdown shortly after their onset due to spanwise instability effects. The instantaneous flow exhibits fine-scale structures which are eliminated in the phase-averaged representation. At this intermediate Reynolds number, a quite complex mixed transitional-turbulent flow field exists which would pose a formidable challenge for its simulation employing simplified approaches.

The effect of structural compliance on the unsteady flow past a membrane airfoil at low Reynolds number ($Re_c = 2.5 \times 10^3$) has been explored by solving the coupled fluid-structural system. The most notable effect of membrane flexibility is the introduction of a mean camber due to the fluid forces acting on both sides of the airfoil. At high incidence, large membrane fluctuations are also established with peak-to-peak amplitudes commensurate with the mean deflection. This dynamic behavior provides an aeroelastically induced excitation of the separated shear layer which rolls up more readily and remains closer to the membrane. These combined effects result in an increase in lift and in a delay in the onset of stall. At a higher Reynolds number ($Re_c = 4.85 \times 10^4$), the inclusion of transition effects is required to capture the correct membrane structural response.

References

Anderson DA, Tannehill JC, Pletcher RH (1984) Computational fluid mechanics and heat transfer. McGraw-Hill Book Company

Dubeif Y, Delcayre F (2000) On coherent-vortex identification in turbulence. J Turbul 1(11):1–22

Ellington C, van den Berg C, Willmott A, Thomas A (1996) Leading-edge vortices in insect flight. Nature 384:626–630

Fung YC (1993) An introduction to the theory of aeroelasticity. Dover, New York

Galbraith M (2009) Implicit large-eddy simulation of low-Reynolds-number transitional flow past the SD7003 airfoil. MS Thesis, Dept of Aerospace Engineering, University of Cincinnati, Cincinnati, OH, March 2009

Galbraith M, Visbal M (2008) Implicit large eddy simulation of low Reynolds number flow past the SD7003 airfoil. AIAA Paper 2008-0225, 2008

Gaitonde DV, Visbal MR (1998) High-order schemes for Navier–Stokes equations: algorithm and implementation into FDL3DI. Technical report AFRL-VA-WP-TR-1998-3060, Air Force Research Laboratory, Wright-Patterson AFB

Gaitonde DV, Shang JS, Young JL (1999) Practical aspects of higher-order numerical schemes for wave propagation phenomena. Int J Numer Methods in Eng 45:1849–1869

Gordnier RE (2008) High fidelity computational simulation of a membrane wing airfoil. AIAA-2008-0614, January 2008

Gordnier RE, Attar PJ (2009) Implicit LES simulations of a low Reynolds number flexible membrane airfoil. AIAA-2009-0579, January 2009

Lele SK (1992) Compact finite difference schemes with spectral-like resolution. J Comput Phys 103:16–42

Lian Y, Shyy W (2006) Laminar-turbulent transition of a low-Reynolds-number rigid or flexible airfoil. AIAA-2006-3051, June 2006

Mathew J, Lechner R, Foysi H, Sesterhenn J, Friedrich R (2003) An explicit filtering method for LES of compressible flows. Phys Fluids 15(8):2279–2289

McGowan G, Gopalarathnam A, OL M, Edwards J, Fredberg D (2008) Computation vs. experiment for high-frequency low-Reynolds-number airfoil in pitch and plunge. AIAA Paper 2008-0653, 2008

Melville RB, Morton SA, Rizzetta DP (1997) Implementation of a fully-implicit, aeroelastic Navier–Stokes solver. AIAA 97-2039, June 1997

Mueller TJ (1985) Low Reynolds number vehicles. AGARDograph No. 288

Ol MV, McAuliffe BR, Hanff ES, Scholz U, Khler C (2005) Comparison of laminar separation bubble measurements on a low Reynolds number airfoil in three facilities. AIAA Paper 2005-5149, 2005

Radespiel R, Windte J, Scholz U (2006) Numerical and experimental flow analysis of moving airfoils with laminar separation bubbles. AIAA Paper 2006-501, 2006

Rojratsirikul P, Wang Z, Gursul I (2008) Unsteady aerodynamics of membrane airfoils. AIAA-2008-0613, January 2008

Shyy W (2008) Aerodynamics of low Reynolds number flyers. Cambridge University Press, New York

Shyy W, Smith R (1997) A study of flexible airfoil aerodynamics with application to micro aerial vehicles. AIAA-1997-1933, June 1997

Smith R, Shyy W (1995) Computation of unsteady laminar flow over a flexible two-dimensional membrane wing. Phys Fluids 7(9):2175–2184

Song AJ, Breuer KS (2007) Dynamics of a compliant membrane as related to mammalian flight. AIAA-2007-0665, January 2007

Steger JL (1978) Implicit finite-difference simulation of flow about arbitrary two-dimensional geometries. AIAA J 16(7):679–686

Stolz S, Adams N (1999) An approximate deconvolution procedure for large-eddy simulation. Phys Fluids 11(7):1699–1701

Vinokur M (1974) Conservation equations of gasdynamics in curvilinear coordinate systems. J Comput Phys 14:105–125

Visbal M (2009) High-fidelity simulation of transitional flows past a plunging airfoil. AIAA Paper 2009-391, 2009

Visbal MR, Gaitonde DV (1999) High-order accurate methods for complex unsteady subsonic flows. AIAA J 37(10):1231–1239

Visbal MR, Gaitonde DV (2002) On the use of high-order finite-difference schemes on curvilinear and deforming meshes. J Comput Phys 181:155–185

Visbal MR, Rizzetta DP (2002) Large-eddy simulation on curvilinear grids using compact differencing and filtering schemes. J Fluids Eng 124:836–847

Visbal MR, Morgan PE, Rizzetta DP (2003) An Implicit LES approach based on high-order compact differencing and filtering schemes. AIAA Paper 2003-4098, June 2003

Waszak MR, Jenkins LN, Ifju P (2001) Stability and control properties of an aeroelastic fixed wing micro aerial vehicle. AIAA-2001-4005, August 2001

Yuan W, Khalid M, Windte J, Scholz U, Radespiel R (2005) An investigation of low-Reynolds-number flows past airfoils. AIAA Paper 2005-4607, 2005

20